

# Effect of molecular hydrogen self-shielding modeling on galaxy formation in cosmological simulation

THỊNH HỮU NGUYỄN<sup>1,2</sup> AND KIRK S. S. BARROW<sup>1</sup>

<sup>1</sup>Department of Astronomy, University of Illinois at Urbana-Champaign, Urbana, IL 61801, USA

<sup>2</sup>Center for AstroPhysical Surveys, National Center for Supercomputing Applications  
Urbana, IL 61801, USA

## ABSTRACT

**Keywords:** Astronomical simulations(1857) — Radiative transfer simulations(1967) — Galaxy formation(595) — Reionization(1383)

### 1. INTRODUCTION

Molecular hydrogen is a building block for star formation. For a gas cloud to collapse into a star, the cloud's self-gravity must be sufficiently large to overcome its pressure gradient. In the absence of other environmental effects, to achieve the collapse, the gas cloud usually needs to have sufficient mass or a high enough cooling rate so that the cooling time is smaller than the free-fall time. Since the cooling time generally decreases when the gas density increases during the collapse, this leads to catastrophic cooling and the gas pressure being lost against gravity, resulting in a collapse. Depending on the temperature and density, there are multiple radiative cooling mechanisms for a cloud to release its internal energy. For primordial gas clouds with atomic hydrogen HI being the dominant component, Bremsstrahlung emission, atomic hydrogen's recombination, collisional ionization, and collisional excitation processes can help cool the gas down to at best the virial temperature of  $10^4 K$ , below which the cooling rate is too low (Thoul & Weinberg 1995). **Elaborate in what condition (temperature, density) molecular hydrogen forms from atomic hydrogen.** However, if molecular hydrogen  $H_2$  is available, it can further stimulate cooling by opening up new cooling channels through its rotational and vibrational energy levels. This allows the gas to cool to  $\approx 100$  Kelvin degrees (Galli & Palla 1998), making it possible for the cloud to collapse into stars. This connection between star formation and  $H_2$  can be reflected through the Kennicutt-Schmidt law (Schmidt 1959; Kennicutt 1998) and various observational evidence in nearby disk galaxies (Wong & Blitz 2002; Kennicutt et al. 2007; Leroy et al. 2013).

Ultraviolet (UV) radiation emitted by nearby active stars can photodissociate molecular hydrogen via the Solomon process (Solomon 1965 - private communica-

tion reported in Field et al. 1966, Stecher & Williams 1967). When absorbing a Lyman-Werner (LW) photon (11.2-13.6 eV), a molecular hydrogen molecule is excited from the ground state to an excited electronic state. Instead of radiatively decaying back to the bound state, about 15 percent of the molecules have their electrons decay into the vibrational continuum, which subsequently dissociates the molecule into atomic hydrogen. Dissociation rates through this mechanism can be inhibited through  $H_2$  self-shielding, a phenomenon where the column density is large enough that the  $H_2$  in the cloud's outer layer absorbs the LW radiation and hence shields the inner region. Previous studies point out the importance of including self-shielding in preserving the amount of molecular hydrogen required for star formation. When simulating a disc galaxy, (Christensen et al. 2012) notices an increase in the amount of cold gas and a clumpier interstellar medium when incorporating self-shielding in their simulation. Safranek-Shrader et al. (2017) finds that self-shielding is crucial in the development of  $H_2$  in the disc's mid-plane, which accounts for 10-15 percent of the total gas mass. Therefore, the hydrogen self-shielding mechanism becomes pivotal in preserving the amount of molecular hydrogen and regulating star formation.

Through modeling a semi-infinite, static slab of gas irradiated on one surface, Draine & Bertoldi (1996) proposes an analytical expression to model  $H_2$  self-shielding factor that includes the effect of line overlap (do we need to elaborate this? also do we need to show the equation here). Maybe show all the papers that use this expression? Look at Hartwig+2015 for the list As shown in Equation (37) of Draine & Bertoldi (1996), the self-shielding factor is a function of the  $H_2$  column density. In the past, computing the column density for multiple 3D directions was

prohibitively computationally expensive (Shang et al. 2010; Wolcott-Green et al. 2011). Therefore, multiple methods have been suggested to approximate the self-shielding effect while trying to alleviate its demanding computational cost. A method is to define a local characteristic length scale across which the  $H_2$  number density is constant. This characteristic length can be either the Jeans length (Shang et al. 2010; Johnson et al. 2011), the Sobolev length (Sobolev 1957; Yoshida et al. 2006), or the Sobolev-like length that is computed from the density-gradient (Gnedin et al. 2009; Gnedin & Kravtsov 2011). Rather than a single characteristic length, Hartwig et al. (2015a) approximates the 3D column densities by creating spherical maps of the column density around each Voronoi cell with 48 equal-area pixels and also taking into account the Doppler effect from the relative velocities of the infalling gas particles. Another non-local method is the six-ray approximation (Yoshida et al. 2003, 2007; Glover & Mac Low 2007a,b), where the  $H_2$  column density is integrated along six directions along three Cartesian axes centered at each particle's position.

However, there are limitations to the applicability of approximate treatments in various test problems when compared to the accurate full ray-tracing calculation. In the context of photodissociation of  $H_2$  in protogalaxies and direct-collapse black hole formation, Wolcott-Green et al. (2011) show that the Sobolev length, the density gradient, and the six-ray approximation methods overestimate the  $H_2$  shielding degree by an order of magnitude in low-density regions of  $n < 10^4 \text{ cm}^{-3}$ . Also in the context of direct-collapse black hole, when comparing with their non-local approximation detailed in Hartwig et al. (2015a), Hartwig et al. (2015b) find that the Jeans approach returns a critical flux value  $J_{\text{crit}}$  - the lowest flux required for a halo with virial temperature above  $10^4 \text{ K}$  to collapse to a supermassive black hole seed - two times larger than the non-local approximation, leading to a disparity in the predicted number density of black hole seeds. Greif (2014) investigate the collapse of primordial star-forming clouds with an accurate  $H_2$  line emission model and notice that the Sobolev method brings about a thermal instability for the collapsing cloud and an order-of-magnitude overestimation of the escape fraction for high optical depth. When evaluating the triggered Population III star formation at the limb of the HII region, Chiaki & Wise (2023) find that while the density-gradient method matches well with the ray-tracing method, the Jeans length approximation results in an overestimation of the number of the Population III stars at the front of the shock wave. The authors suggest that this is because the thickness of the

$H_2$  ring of the shock front is typically smaller than the Jeans length, and thus the local approximation is inappropriate. In their large-scale galactic discs simulations, Safranek-Shrader et al. (2017) notices that the Sobolev method underpredicts the  $H_2$  abundance in the disc by a factor of 5, while the six-ray and the Jeans length methods perform better, which is contrary to the findings that Jeans length method is ineffective in previous studies. Thus, the validity of these approximation methods is highly problem-dependent and they cannot be used as a general substitution for the full ray-tracing calculation.

#### A simulation that uses approximated H2 self-shielding: COLDSDIM, Maio et al 2021

In this paper, we expand the investigation by comparing these approximation methods with the detailed ray-tracing methods, this time in the context of star formation during the Reionization period. This will help further examine and inform the community about the applicability of these approximations in modeling  $H_2$  in different contexts. In Section ..., we will describe our simulation and the implemented  $H_2$  self-shielding models. Section ... analyzes the effect of these models on star formation and galaxy evolution during Reionization. Last but not least, in Section ..., we discuss the implications of the findings and summarize the paper.

Maybe a paragraph at the beginning about the observational and theoretical evidence of the relation between  $H_2$  and star formation (Kenicutt-Schmidt relation, for example)? I think this is a good idea. I'm happy to help with this part if you need some background.

## 2. METHOD

### 2.1. Cosmological simulations

We run and analyze outputs from a radiation-hydrodynamic adaptive mesh refinement simulation ENZO (Bryan et al. 2014). Two sets of cosmological simulations are generated to explore the self-shielding effect in the early stage and in the late stage of the Reionization period, which we will refer to as *EarlyRe* and *LateRe*, respectively. In the early stage of Reionization, the UV background radiation is still local. Thus, the *EarlyRe* set provides a control sample to study whether the self-shielding approximation affects the overall star formation activity during a low non-local UV-radiation scenario. On the other hand, the *LateRe* allows us to study how the resistance of molecular clouds against a strong photoionization background depends on the self-shielding treatments. Both sets assume a flat  $\Lambda$ CDM cosmology and are run with

the cosmological parameters obtained from Planck Collaboration et al. (2016):  $\Omega_M = 0.3065$ ,  $\Omega_\Lambda = 0.6935$ ,  $\Omega_b = 0.0483$ ,  $h = 0.679$ ,  $\sigma_8 = 0.8154$ , and  $n = 0.9681$ . The total moving volume of the EarlyRe and LateRe simulations are  $13 \text{ (Mpc/h)}^3$  and  $5 \text{ (Mpc/h)}^3$ , respectively. Both sets have the root grid dimension of  $256^3$ . The total number of dark matter particles is  $\approx 10^{7.82}$  particles for the EarlyRe set and  $\approx 10^8$  particles for the LateRe set. Inside the total volume of the EarlyRe (LateRe) simulation, we create a smaller zoom-in region using three (check the MUSIC file of LateRe) additional levels of nested refinement to create an effective grid size resolution of  $2632.5 \times 2512.9 \times 2871.9 \text{ kpc}^3$  ( $920.5 \times 1564.8 \times 1196.6 \text{ comoving kpc}^3$ ) at the last snapshot at redshift of 10.9 (6.4). In the zoom-in region, the most refined dark matter particle mass is  $2.7 \times 10^4$  ( $1.5 \times 10^3$ )  $M_\odot$ . As the density passes a certain threshold, the grids inside this zoom-in region can further be refined adaptively up to  $2^{13}$  ( $2^{14}$ ) times the root grid dimensions. This allows a maximum spatial resolution down to 3.07 pc (1.89 pc) at the last time step, which allows the tracking of large molecular clouds through initial collapse. We use radiative star cluster particle (Wise & Cen 2009) and Population III star particle (Abel et al. 2007) for our star formation prescription.

Each set contains a version running with detailed ray-tracing calculation (EarlyRe-ray and LateRe-ray) and a version running with a local approximation of the column density (EarlyRe-apx and LateRe-apx) when computing the  $H_2$  self-shielding factor. The self-shielding model is set by the RadiativeTransferOpticallyThinH2 ENZO radiation parameter, where a value of 1 enables an optically thin  $H_2$  dissociating Lyman-Werner radiation field and a value of 0 uses ray-tracing for the calculation. For the EarlyRe simulation set, the EarlyRe-ray and the EarlyRe-apx are initialized with an identical list of parameters and initial conditions except for the RadiativeTransferOpticallyThinH2 parameter. We evolve the two simulations from  $z = 100$  to  $z \approx 10.9$ , each output is 1 Myr apart. For the LateRe set, to save computational time, we run the two simulations without ray-tracing until  $z \approx 7.3$ , then we switch the RadiativeTransferOpticallyThinH2 parameter to 0 for one of the simulations (the LateRe-ray) and run both of them until  $z \approx 6.4$ . This allows us to examine the effect of self-shielding near the end of the reionization epoch.

## 2.2. Halo tracking and merger tree algorithms

To identify the halos in the simulations, we employ SHINBAD (Barrow et al 2025, in preparation), an all-in-one algorithm that both finds halos and builds merger trees based on robust energy definition and particle

tracking of dark matter particles. (Note that this is version 1088 of SHINBAD, ask Kirk how to expand this part). We exclude all the halos that are outside the refined region of the simulation box - the region containing only the highest and the second-most highest resolution dark matter particles - to ensure that the halos are physical.

### 2.3. Numerical $H_2$ self-shielding models

A  $H_2$  self-shielding process happens when a molecular cloud has a sufficiently high column density that its outer layer absorbs all the Lyman-Werner UV photons, effectively shielding the molecules within it against photodissociation. Via modeling a semi-infinite, static slab of gas that is irradiated on one surface, Draine & Bertoldi (1996) express a self-shielding-accounted photodissociation rate as

$$k_{\text{diss}}(N_{H_2}, T) = f_{sh}(N_{H_2}, T) \cdot k_{\text{diss}}(N_{H_2} = 0, T), \quad (1)$$

where  $f_{sh}(N_{H_2}, T)$  is a self-shielding factor or shielding function, and  $k_{\text{diss}}(N_{H_2} = 0, T)$  is the dissociation rate in a optically-thin regime. At a low temperature (hundreds of K), the self-shielding factor can be approximately computed from only the  $H_2$  column density,

$$f_{sh} = \min \left[ 1, \left( \frac{N_{H_2}}{10^{14} \text{ cm}^{-2}} \right)^{-3/4} \right]. \quad (2)$$

This is controlled by setting the ENZO radiation parameter RadiativeTransferH2ShieldType = 0, which is also its default value. We use this expression to calculate the self-shielding factor in the EarlyRe-apx simulation. It is important to note that the convention of  $f_{sh}$  value is slightly counter-intuitive: the  $f_{sh}$  value of 0 means full self-shielding is available, and the  $f_{sh}$  value of 1 means there is no self-shielding. We also acknowledge that Draine & Bertoldi (1996) lists a more accurate formula to calculate  $f_{sh}$  that takes temperature as a parameter. However, using this formula does require additional computational resources that we save to run the ray-tracing scheme. Thus, we choose to use the approximated expression at low temperatures. Check Gnedin and Draine 2014, where they do a comparison between this equation with a more accurate one (including line overlap). Summarize their results here.

Maybe talking about the limitations of Draine and Bertoldi 1996, as on page 5, right column of Wolcott-Green.

To avoid the high computational expense of finding the  $H_2$  column density in multiple 3D directions, previous studies employ different techniques to approximate

it (see Section 1). In this paper, we compare the results from two methods: a direct integration from ray tracing and a Sobolev-like length approximation (Gnedin et al. 2009; Wolcott-Green et al. 2011). Even though demanding more computational time, the ray tracing treatment ensures a more accurate radiative transfer calculation. ENZO uses the adaptive ray tracing technique (Wise & Abel 2011) that is based on the HEALPix (Hierarchical Equal Area isoLatitude Pixelation, Gorski et al. 2005) scheme. The column density is integrated along a HEALPix rays,

$$N_{H_2} = \int n(H_2)ds. \quad (3)$$

The Sobolev-like treatment is a local approximation in which the number density  $n_{H_2}$  is assumed to be constant within a characteristic length scale  $L_{\text{char}}$ . In the Sobolev-like approximation, the characteristic length scale is defined as a distance over which the cell's gas density  $\rho$  diminishes. The gas beyond this distance is sparse enough that its influence on shielding is negligible, and thus molecular hydrogen is dissociated in an optically thin fashion. The column density is then computed by

$$N_{H_2} \approx n_{H_2} L_{\text{char}} = n_{H_2} \frac{\rho}{|\nabla \rho|} \quad (4)$$

The approximation is enabled by setting the ENZO parameters `RadiativeTransferOpticallyThinH2 = 1` and `RadiationShield = 2`.

Figure 1 compares the self-shielding factor  $f_{sh}$  between the ray-tracing model and the Sobolev-like approximation model. At the time step corresponding to  $z = 10.9$ , we select 31 halos that contain stars or overlap with another halo that contains stars. For each halo, we select two gas cells to evaluate the self-shielding factor: (1) the gas cell with the highest gas density, and (2) the gas cell with the highest gas density gradient. Each scatter point in Figure 1 represents a selected gas cell. In the approximation model, the self-shielding factor of a gas cell is calculated using Equations 2 and 3. For the ray-tracing model, since the simulation output does not store the photodissociation rate calculation, we need to re-compute the self-shielding factor using Equation 2 with an attenuated LW flux-weighted average column density. The LW flux from each star to a selected gas cell is calculated as follows. Firstly, the intrinsic spectrum of a star particle is generated using the Flexible Stellar Population Synthesis (fsps) with the age and metallicity of the star particle as inputs. We assume an initial mass function from Davé (2008) evaluated at  $z = 0$ , and we use the MIST isochrone library and MILES spectral library to generate the spectra. **may cite Susie's paper**

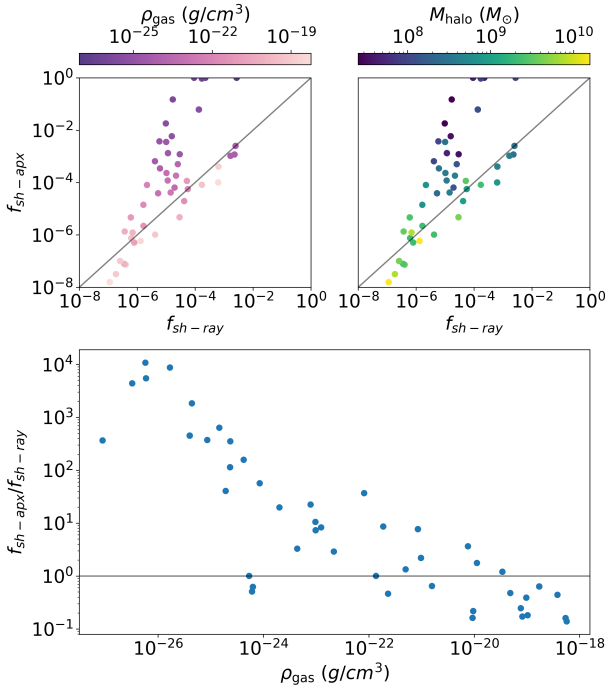
**here or ask her for more information.** Then, we calculate the attenuation by including both scattering and absorption due to H/He and metals **Ask Kirk to include how the absorption and scatterings are computed.** With the scattering and absorption coefficients, we can compute the total optical depth and then the attenuation of the stellar spectrum from the source to the target gas cell. Lastly, we calculate the attenuated flux of each source to the gas cell, compute the LW flux-weighted average  $H_2$  column density, and get the self-shielding factor from the ray-tracing model. It is important to note that we only include stars within the halo's virial radius to estimate the flux-weighted average  $H_2$  density because stars outside the radius are too far from the selected gas cell to contribute considerably to the total flux at the selected gas cell.

Figure 1 demonstrates a clear disparity in the  $f_{sh}$  value between EarlyRe-apx and EarlyRe-ray. In particular, the approximation model tends to overestimate the amount of shielding for cells with a gas density larger than  $10^{-20} g/cm^3$  by up to 1 dex. On the other hand, diffuse gas is subjected to underestimated  $H_2$  self-shielding when the Sobolev-like approximation model is used. For highly diffuse gas, this underestimation can be up to 3–4 dex. This connection between gas density and  $f_{sh}$  implies a mass-dependent effect of the self-shielding approximation model on halos. The top right subfigure of Figure 1 shows that larger halos ( $M_{\text{halo}} > 10^{9.5} M_{\odot}$ ) have their molecular cloud region over-shielded in the approximation model because the gas is denser. On the other hand, the molecular clouds in small halos ( $M_{\text{halo}} < 10^{8.5} M_{\odot}$ ) are under-shielded against LW radiation when using the Sobolev-like approximation. In some cases, the approximation returns no shielding effect even though those gas cells are still weakly shielded ( $f_{sh} \approx 10^{-3}$  when ray-tracing is utilized). Only molecular gas clouds in halos whose mass is about  $10^9 M_{\odot}$  are well modeled in the approximation model. The significance of this effect on star formation will be explored in Section 3.1.

**Maybe a comparison in terms of the time run between the two methods**

#### 2.4. Cross-matching halos

To examine how each individual halo is affected by the implementation scheme of  $H_2$  self-shielding, we perform cross-matching between halos in the simulations with ray-tracing (*EarlyRe-ray* and *LateRe-ray* sets) and their counterparts in the simulations with the Sobolev-like approximation (*EarlyRe-apx* and *LateRe-apx* sets).



**Figure 1.** The comparison between the self-shielding factor between the *EarlyRe-ray* and the *EarlyRe-apx* simulation, evaluated at  $z = 10.9$ . Two gas cells with the highest gas density and highest gas density gradients are chosen in 31 halos in different mass range to evaluate the self-shielding factors. (Top) The relationship between the self-shielding factors calculated by the Sobolev-like approximation model and the ray-tracing model, colored by the cell’s gas density (top left) and the host halo’s mass (top right). (Bottom) The ratio between the approximated and the ray-traced self-shielding factors is plotted as a function of gas density. The Sobolev-like approximation tends to overestimate the amount of  $H_2$  self-shielding in the high gas density regime and underestimate it in the low gas density regime.

The matching requirements are

$$\frac{2}{3} < \frac{M_{vir_{ray}}}{M_{vir_{apx}}} < \frac{3}{2}$$

$$\frac{d_{COM}}{R_{vir_{ray}}} < 0.25, \quad \frac{d_{COM}}{R_{vir_{apx}}} < 0.25 \quad (5)$$

The virial mass and radius in Equation 5 come from ROCKSTAR and are calculated using only dark matter. We cross-match all the halos at the last timestep of the simulations and then trace back their merger tree using the **consistent-tree** outputs (details in Subsection 2.2).

## 2.5. Star assignment

We uniquely assign each star particle in the simulation to one dark matter halo in a two-step fashion. For the first step, a star particle is assigned to a halo where it is

first created. If a star particle is created inside the intersection of multiple halos, we will calculate the orbital energy of that star particle with respect to each halo’s center to determine which halo the particle belongs to. The assigned halo is the one with lower relative total orbital energy. We assume that a star particle never leaves its assigned halo unless that halo merges with another one, in which case the star particle will become a member of the descendant halo of the merger. This assumption allows a quick assignment of stars to halos without the need to calculate the orbital energy of each star to multiple halos, which is computationally expensive. The assignment’s first step starts from the first snapshot to the last snapshot of the simulation.

Even though stars do not generally leave a halo’s potential well for isolated halos, the behavior becomes more complex during halo-halo interaction as stripping can occur and stars can be lost from one halo to another (Kannan et al. 2015). Therefore, the second step of our process is to address this shortcoming of the first step’s assumption and to refine the star assignment result. In this step, we validate the output from the first step and check whether a star remains in its assigned halo’s virial radius throughout its lifetime. If a star escapes the virial radius of its originally assigned halo, we assign that star to a new halo under two conditions: (1) the star’s position must be within the new halo’s virial radius and (2) the star’s total orbital energy with respect to the new halo must be negative. Similar to the first step, if a star is located inside multiple potential new halos, we assign that star to the halo with the lowest negative orbital energy. If either Condition (1) or (2) fails at a certain timestep, this suggests that the star is stripped out of the potential well of all halos and thus we remove that star from the halo assignment process of that time step.

Once each star particle is uniquely associated with one halo, we calculate a halo’s stellar mass and SFR exclusively based on its member star particles. This gravitational unbinding of star particles guarantees that each halo’s stellar mass profile are not overlap and independent of each other.

## 3. RESULTS

### 3.1. Effect on the molecular hydrogen content and star formation

Because the column density approximation model directly concerns the calculation of the molecular hydrogen density, we first investigate the amount of  $H_2$  in the ray tracing and approximation treatment. Figure 2 shows the  $H_2$  fraction ( $f_{H_2}$ ), which is the ratio between the  $H_2$  mass with the total gas mass, as a function of the total halo mass in three snapshots, one at the time

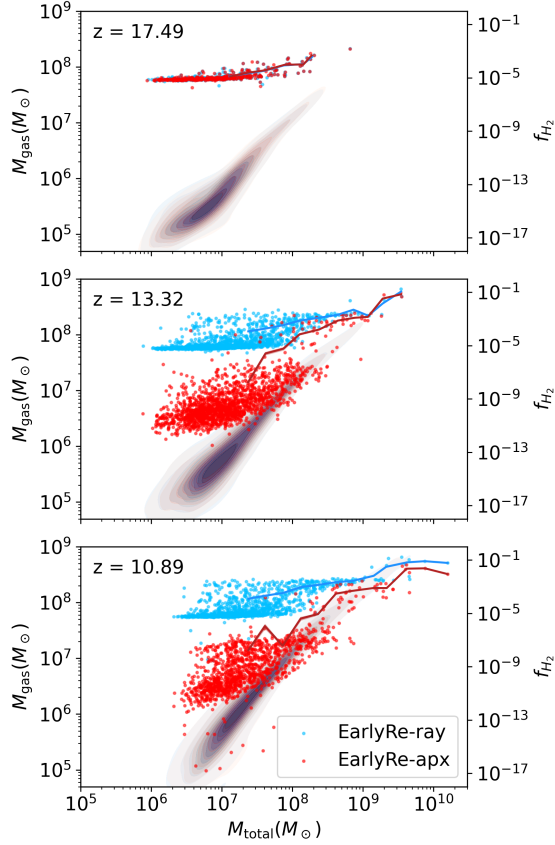


**Figure 2.** The relationship between the  $H_2$  fraction and the total mass in the timestep where stars first appear, in the intermediate, and in the last timestep of the *EarlyRe* dataset. The contour plots show the  $M_{\text{gas}}$  distribution and the scatter points show the  $H_2$  fraction of all halos in the simulation box.

where star particles first appear in the simulations ( $z \approx 17.49$ ), one at the time step in the middle of the simulation run ( $z \approx 13.32$ ), and one being the last time step of the run ( $z \approx 10.9$ ). Each halo in the snapshot is represented by a scatter point, the line represents the running average of each total mass bin, and the shaded region around the line is the standard deviation of the scatter points within each mass bin. The contour plots represent the distribution of the halos in the  $M_{\text{gas}} - M_{\text{total}}$  space. According to Figure 2, both EarlyRe-ray and Early-apx simulations have similar gas mass distribution across all timesteps, showing  $f_{H_2}$  represents the amount of  $H_2$  in the halos. However,  $f_{H_2}$  shows a notable difference between the two radiative transfer treatments, especially at the later time step and in the lower-halo-mass regime. For halo mass smaller than  $10^8 M_{\odot}$ , the  $f_{H_2}$  in the ray-tracing treatment is larger than that of the Sobolev-like approximation treatment by 3 to 6 dex. This difference grows larger as the simulation evolves,

reaching up to 12 dex at the last time step for small halos. The EarlyRe-ray simulation also develops a lower limit for  $f_{H_2}$  of around  $10^{-5}$ , whereas the  $f_{H_2}$  is allowed to reach much further value in the EarlyRe-apx simulation. This shows that the ray-tracing treatment models the self-shielding effect much better and thus helps preserve more molecular hydrogen in the halos. As pointed out in Figure 1, the approximation treatment considerably underestimates  $H_2$  self-shielding in a low gas density regime and molecular hydrogen to get photodissociated more easily, inferring that smaller halos are the most susceptible to the choice of the model. At a higher mass range, the difference in  $f_{H_2}$  between the two models gradually diminishes. This is reasonable because larger halos have deeper gravitational potential well and have more dense cool gas regions where  $H_2$  exists. In these regions, the approximation model matches well with the ray-tracing model (as shown in Figure 1), leading to an agreement of  $f_{H_2}$  between the two runs.

We proceed to investigate whether the self-shielding treatment affects the stellar mass of galaxies in the simulation. Figure 3 shows the relationship between stellar mass and halo mass between the *Early-Ray* and *Early-apx* in the time step where stars first appear (top left panel), in the last time step of the dataset (bottom right panel), and in the intermediate time steps. Figure 4 displays the number of halos that host stars as a function of time for different halo mass bins. The stellar component of the halos is unbound by using the star assignment procedure described in Section 2.5. Even though the number of halos with stars is even between *EarlyRe-apx* and *EarlyRe-ray* in the beginning, there are more halos with stars in *EarlyRe-ray* at the end of the simulation, particularly halos with  $M_{\text{halo}} < 10^9 M_{\odot}$ . For ease of reference and lack of a better term, we will use the term "galaxy" to refer to a halo with stars, as opposed with halos with only gas and dark matter particles. From 375 million years after the Big Bang to near the end of the simulation ( $z \approx 11.88 - 11$ ), there are two to four galaxies more in the simulation with the ray-tracing treatment. Furthermore, at a similar halo mass, smaller halos in *EarlyRe-ray* tend to have more stars than their counterparts in *EarlyRe-ray* by several dex in solar mass. This indicates that the use of Sobolev-like approximation for  $H_2$  self-shielding treatment inhibits star formation activity in small halos and dwarf galaxies. On the other hand, halos whose dark matter mass is larger than  $10^9 M_{\odot}$  show good agreement in stellar mass, suggesting that the stellar components of large halos are unaffected by our choice of  $H_2$  self-shielding model. This observation aligns with Figure 2, where we

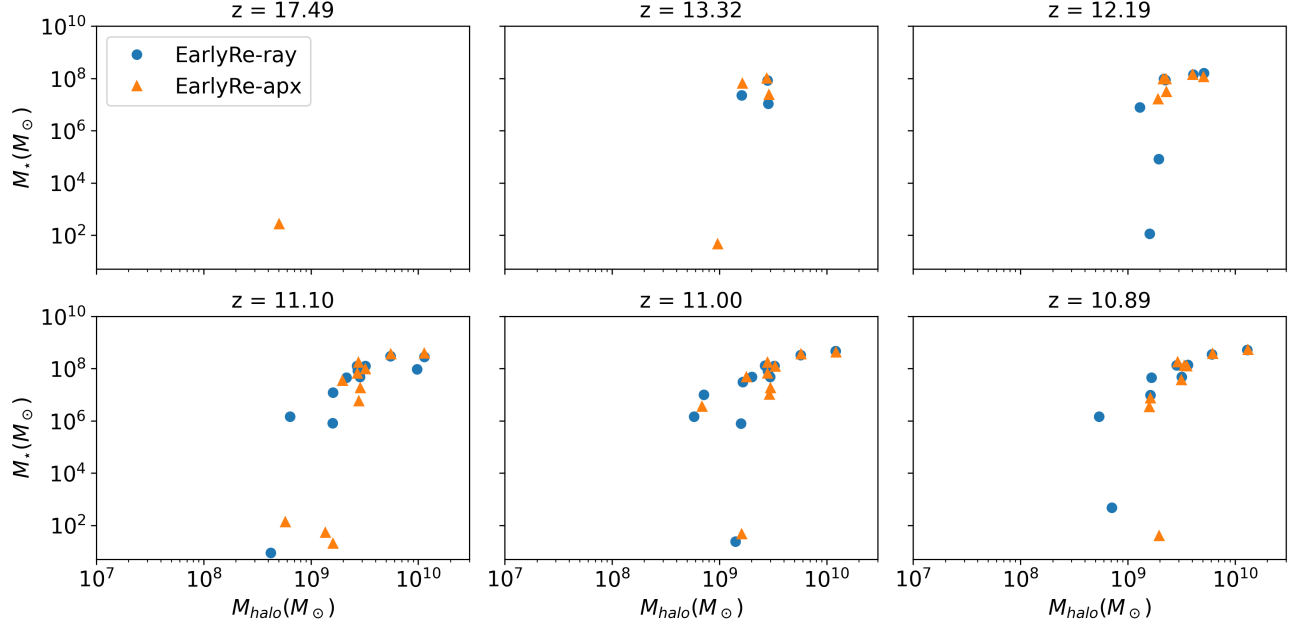


**Figure 3.** The relationships between stellar mass and total mass of all the halos in the timestep where stars first appear, in the intermediate timesteps, and in the last timestep of the *EarlyRe* dataset.

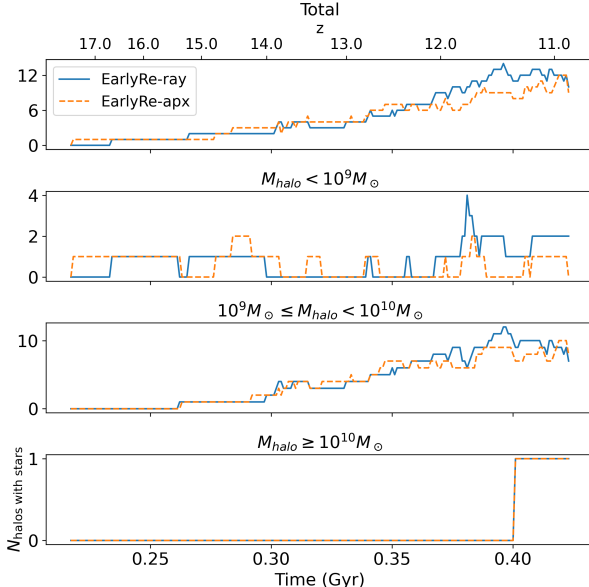


**Figure 4.** The comparison between the number of halos with stars as a function of time for each halo mass bin between the *EarlyRe-ray* and the *EarlyRe-apx* simulations.

see that  $H_2$  is more accurately shielded in higher halo mass in *EarlyRe-apx*.

Another difference between *EarlyRe-ray* and *EarlyRe-apx* is the time when star particles first appear in the simulation. According to Figure 4, the formation of the first galaxy in *EarlyRe-apx* occurs 16 million years before that in *EarlyRe-ray*. The first galaxies in the two simulations both form in a halo with a dark matter mass

smaller than  $10^9 M_\odot$ . This is rather intuitive, given that previous evidence shows that for small halos, stars form easier in the simulation using a ray-tracing model. However, further investigation suggests that the timing discrepancy in the formation of first stars is likely due to a stochastic nature of our star formation prescription rather than a physical reason. Before the first stars appear in a halo in *EarlyRe-apx*, the temperature and density distribution of gas and molecular hydrogen of the counterpart halo in *EarlyRe-ray* are similar to the halo in *EarlyRe-apx*. More discussion and plots regarding the first galaxies in the two simulation will be directed to the Appendix. **Reminder to include the appendix**

### 3.2. Effect on the ISM, CGM, and IGM

Sub-section 3.1 explores how two treatments of modeling  $H_2$  affect star formation in a halo as a whole. In this section, we more closely examine the effect of  $H_2$  self-shielding modeling on the interstellar medium (ISM), the circumgalactic medium (CGM), and the intergalactic medium (IGM) to help further explain the previous observations we have on star formation.

#### 3.2.1. Defining ISM, CGM, and IGM in cosmological simulation

The boundary of the ISM, CGM, and IGM region in our analysis is defined as follows. The ISM region starts from the galaxy's center of mass to  $R_{\text{bary},2000}$ , which is the radius enclosing a baryonic (gas and stars) mass density 2000 times the universe's critical mass density at a certain redshift. The benefit of this approach is to

553 help define the ISM more robustly and more physically  
 554 because it is redshift and density dependent. **Search**  
 555 **for papers that use similar approach.** Depending  
 556 on the redshift and the galaxy's compactness,  $R_{\text{bary},2000}$   
 557 typically ranges from 0.15 to 0.25 times the halo's virial  
 558 radius, which is the common ratio used to define a  
 559 galaxy in a halo in cosmological simulations ([Strawn et al. 2024](#)) **add more citations here.**

561 Also, it is important to note that the baryonic center  
 562 of mass does not always coincide with the halo's center  
 563 of mass. Thus, in some cases, we shift the virial region  
 564 to be centered on the gas and stellar mass instead of the  
 565 dark matter mass; however, this shift is not large and  
 566 does not affect our interpretation.

### 567 3.2.2. Effect on the ISM and CGM

568 **Make a big figure showing all the halo pairs**  
 569 **projection plot at the last snapshot.**

570 **Remember to comment on the stellar mass of**  
 571 **the galaxies in Figure 5 and 6.**

### 572 3.2.3. Effect on the IGM

573 *For the radiative star cluster model and the Population*  
 574 *III star model used in our simulation, their overdensity*  
 575 *thresholds for a star particle to form are  $10^7$  and  $10^6$ ,*  
 576 *respectively. At the time step where we evaluate the  $f_{sh}$*   
 577 *( $z = 10.9$ ), these overdensity thresholds correspond to*  
 578 *a gas density threshold of  $4.5 \times 10^{-20}$  and  $4.5 \times 10^{-21}$ .*  
 579 *According to Figure 1, these thresholds lie in the regime*  
 580 *where  $f_{sh}$  is typically over-estimated in the approxima-*

581 *tion model. On the other hand,  $H_2$  gas in the interstellar*  
 582 *medium (ISM) of EarlyRe-apx can be under-shielded.*

### 583 3.3. Effect on reionization

584 Include the neutral hydrogen fraction Include gas in-  
 585 flow and outflow analysis? -> Use supernova rate in-  
 586 stead

### 587 3.4. Investigation on late reionization period

588 Include the analysis for the LateRe set

## 589 4. CONCLUSIONS AND DISCUSSIONS

590 Maybe mention that the Renaissance Simulation (and  
 591 maybe others) doesn't implement self-shielding, so can  
 592 affect the results.

593 The strong radiation in late reionization destroys H<sub>2</sub>  
 594 in both *ray* and *apx* sets. This is reflected by the fact  
 595 that the separation between the *ray* and the *apx* is not  
 596 as prominent as in the EarlyRe set. In the EarlyRe set,  
 597 the radiation is still weak, thus it only affects the non-  
 598 shielding version. The halos of *ray* version are shielded  
 599 with this weak radiation, but not with the strong radi-  
 600 ation as in LateRe.

601 **Remember to use bullet points for each main**  
 602 **result and specifically state the figure associated**  
 603 **with each main result.**

604 Acknowledgement: —

## REFERENCES

- 605 Abel, T., Wise, J. H., & Bryan, G. L. 2007, The  
 606 Astrophysical Journal, 659, L87, doi: [10.1086/516820](https://doi.org/10.1086/516820)
- 607 Bryan, G. L., Norman, M. L., O'Shea, B. W., et al. 2014,  
 608 The Astrophysical Journal Supplement Series, 211, 19,  
 609 doi: [10.1088/0067-0049/211/2/19](https://doi.org/10.1088/0067-0049/211/2/19)
- 610 Chiaki, G., & Wise, J. H. 2023, Monthly Notices of the  
 611 Royal Astronomical Society, 520, 5077,  
 612 doi: [10.1093/mnras/stad433](https://doi.org/10.1093/mnras/stad433)
- 613 Christensen, C., Quinn, T., Governato, F., et al. 2012,  
 614 Monthly Notices of the Royal Astronomical Society, 425,  
 615 3058, doi: [10.1111/j.1365-2966.2012.21628.x](https://doi.org/10.1111/j.1365-2966.2012.21628.x)
- 616 Davé, R. 2008, Monthly Notices of the Royal Astronomical  
 617 Society, 385, 147, doi: [10.1111/j.1365-2966.2008.12866.x](https://doi.org/10.1111/j.1365-2966.2008.12866.x)
- 618 Draine, B. T., & Bertoldi, F. 1996, The Astrophysical  
 619 Journal, 468, 269, doi: [10.1086/177689](https://doi.org/10.1086/177689)
- 620 Field, G. B., Somerville, W. B., & Dressler, K. 1966,  
 621 Annual Review of Astronomy and Astrophysics, 4, 207,  
 622 doi: [10.1146/annurev.aa.04.090166.001231](https://doi.org/10.1146/annurev.aa.04.090166.001231)
- 623 Galli, D., & Palla, F. 1998, Astronomy and Astrophysics,  
 624 335, 403, doi: [10.48550/arXiv.astro-ph/9803315](https://doi.org/10.48550/arXiv.astro-ph/9803315)
- 625 Glover, S. C. O., & Mac Low, M.-M. 2007a, The  
 626 Astrophysical Journal Supplement Series, 169, 239,  
 627 doi: [10.1086/512238](https://doi.org/10.1086/512238)
- 628 —. 2007b, The Astrophysical Journal, 659, 1317,  
 629 doi: [10.1086/512227](https://doi.org/10.1086/512227)
- 630 Gnedin, N. Y., & Kravtsov, A. V. 2011, The Astrophysical  
 631 Journal, 728, 88, doi: [10.1088/0004-637X/728/2/88](https://doi.org/10.1088/0004-637X/728/2/88)
- 632 Gnedin, N. Y., Tassis, K., & Kravtsov, A. V. 2009, The  
 633 Astrophysical Journal, 697, 55,  
 634 doi: [10.1088/0004-637X/697/1/55](https://doi.org/10.1088/0004-637X/697/1/55)
- 635 Gorski, K. M., Hivon, E., Banday, A. J., et al. 2005, The  
 636 Astrophysical Journal, 622, 759, doi: [10.1086/427976](https://doi.org/10.1086/427976)
- 637 Greif, T. H. 2014, Monthly Notices of the Royal  
 638 Astronomical Society, 444, 1566,  
 639 doi: [10.1093/mnras/stu1532](https://doi.org/10.1093/mnras/stu1532)

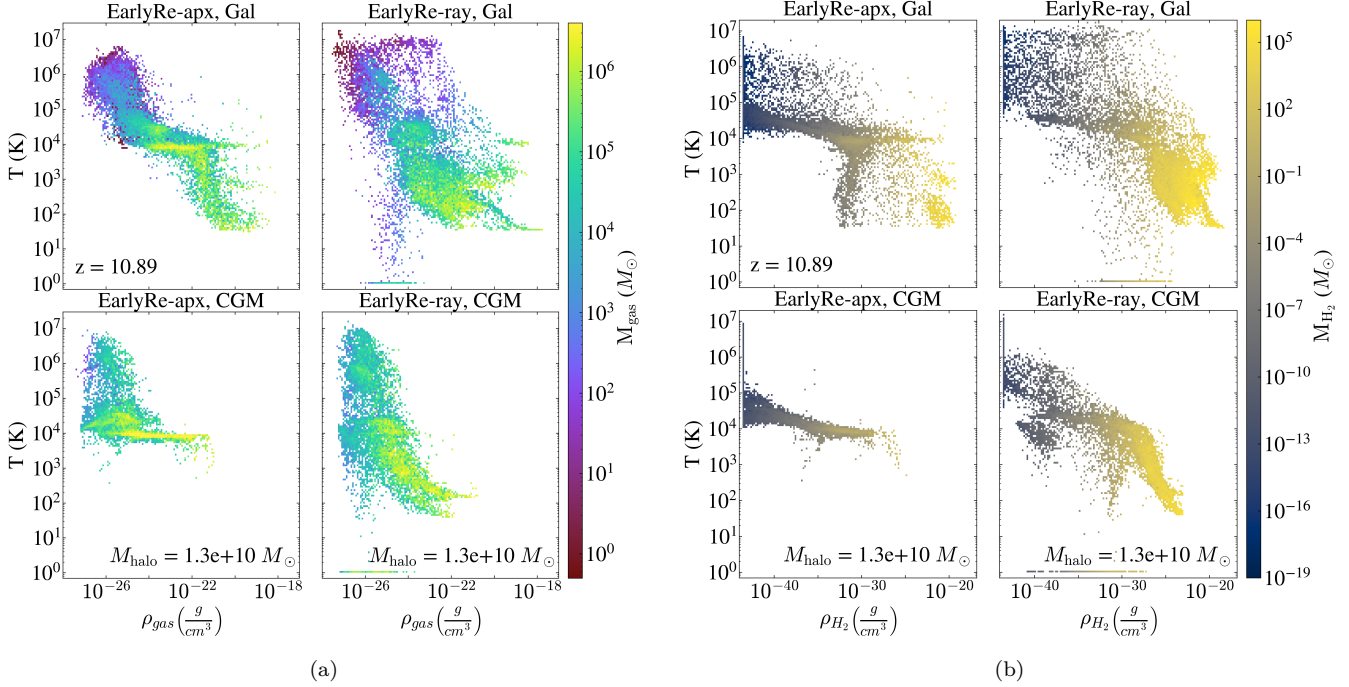


**Figure 5.** The gas phase plot (Sub-figure (a)) and the molecular hydrogen phase plot (Sub-figure (b)) of the largest halo ( $M_{\text{halo}} = 1.3 \times 10^{10} M_{\odot}$ ) in our simulation set, evaluated at the last time step  $z = 10.89$ . For each sub-figure, the left column shows the halo in *EarlyRe-apx*, and the right column shows its counterpart in *EarlyRe-ray*. The top row in each subfigure shows the phase plot using the gas cells within the galaxy region ( $r \leq R_{\text{bary},2000}$ ), and the bottom row shows the phase plot using the gas cells in the CGM region ( $R_{\text{bary},2000} < r \leq R_{\text{vir}}$ ).

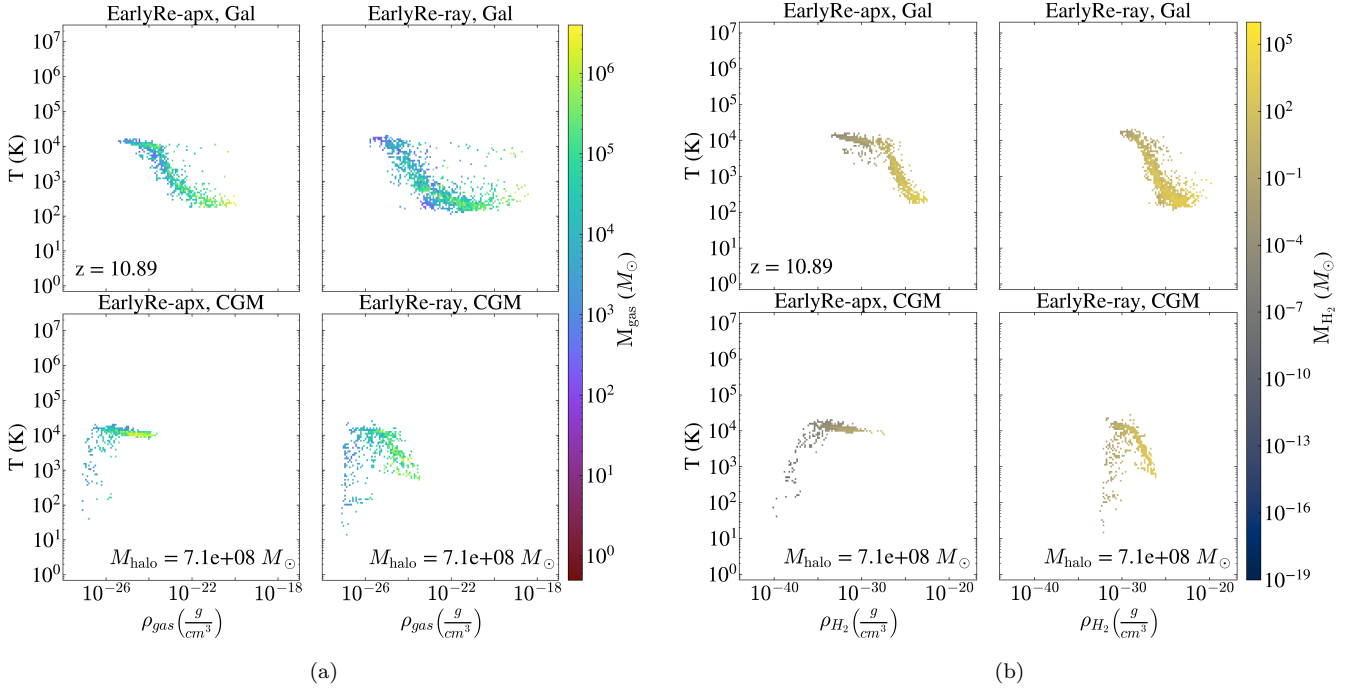


**Figure 6.** Similar to Figure 5, for a halo with mass  $M_{\text{halo}} = 7.1 \times 10^8 M_{\odot}$ .

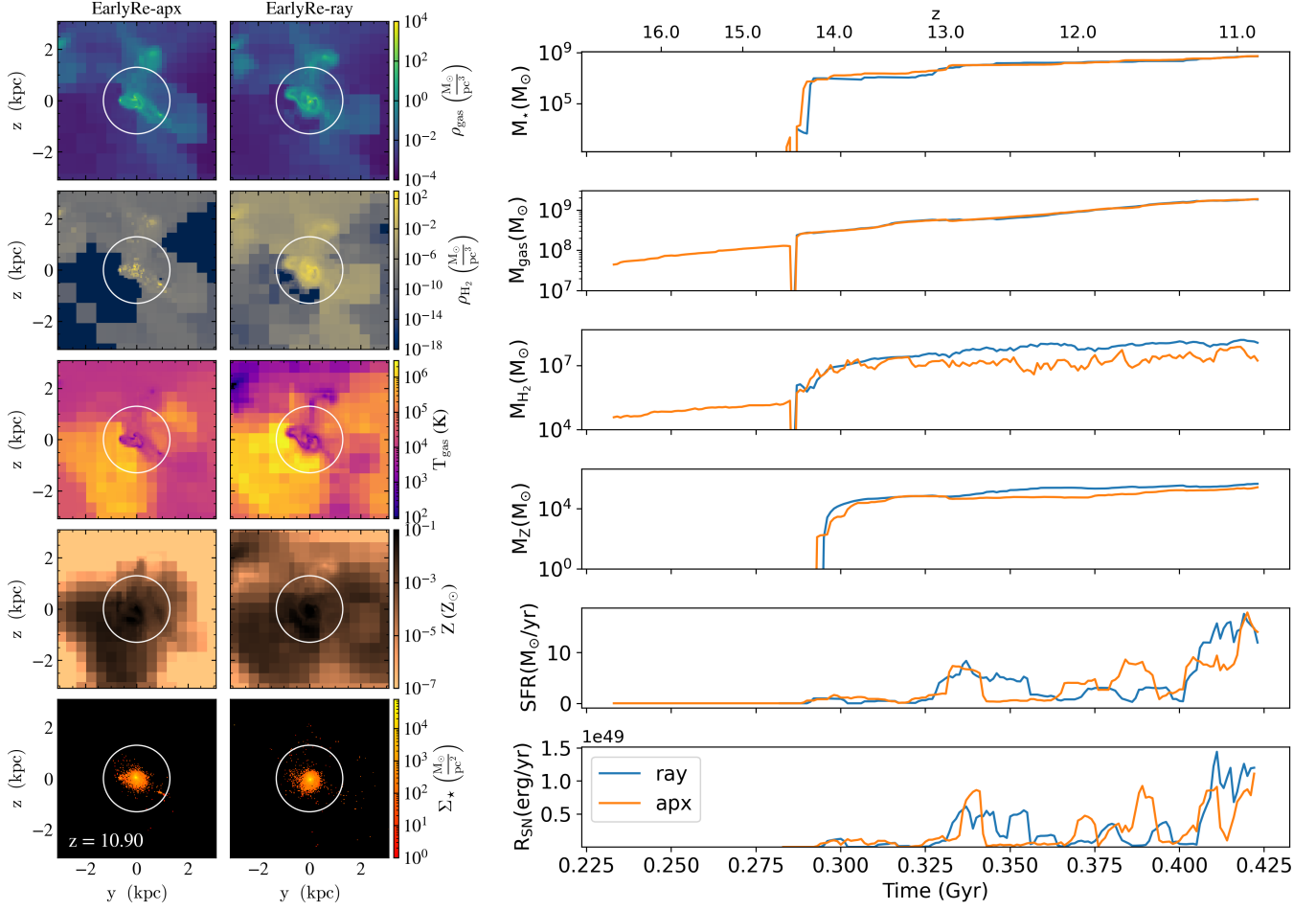


**Figure 7.** (Left) The gas density,  $H_2$  density, temperature, metallicity, and stellar surface density projection plot of Halo 0 within one virial radius. The white circle represents the boundary of the galaxy, which is defined as the radius enclosing the baryonic density 2000 times larger than the critical density of the universe. (Right) The time evolution of different properties in Halo 0 between the *EarlyRe-ray* and *EarlyRe-apx* simulations.

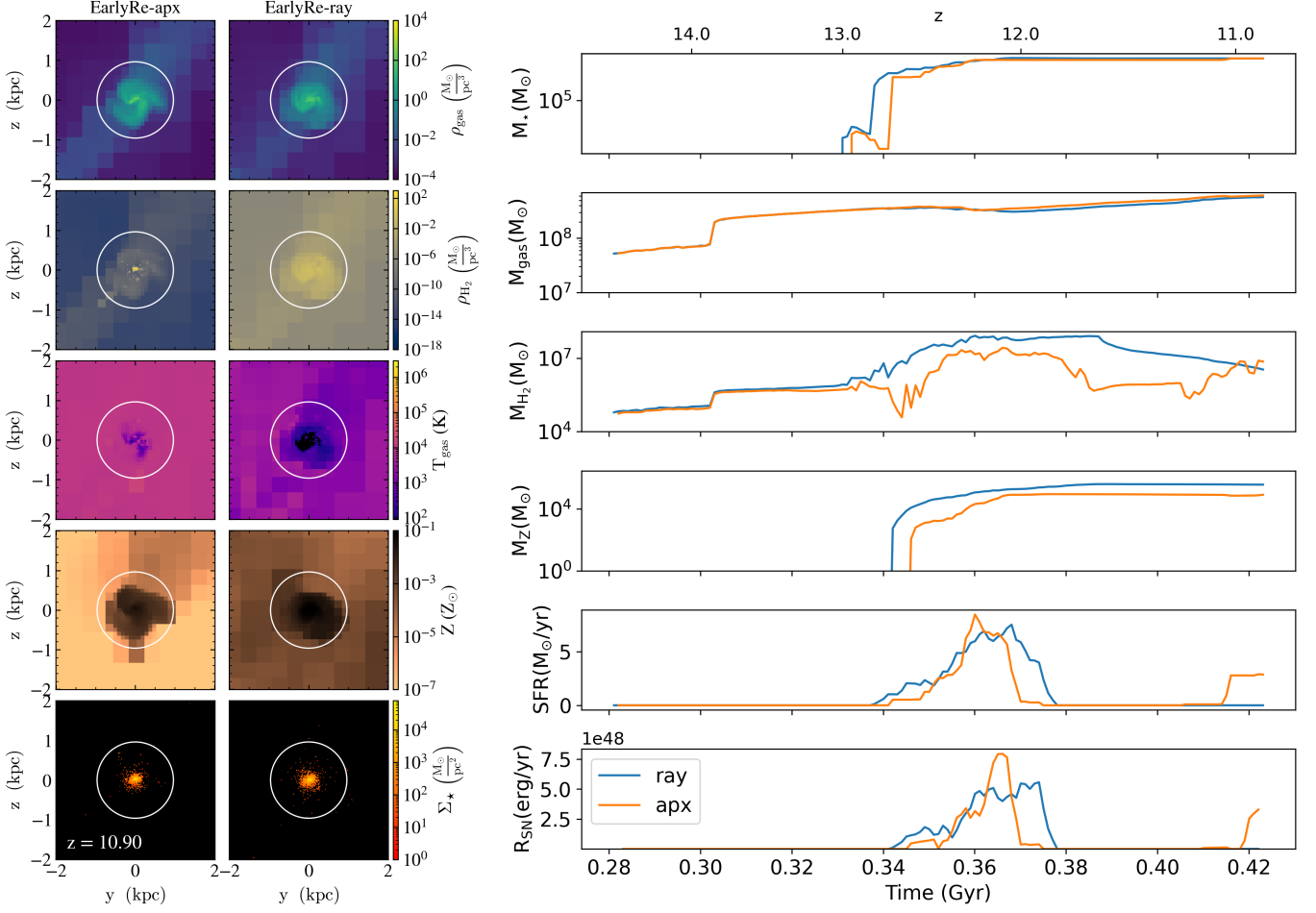


**Figure 8.** Same as Figure 7, but for another Halo.

- 640 Hartwig, T., Clark, P. C., Glover, S. C. O., Klessen, R. S.,  
 641 & Sasaki, M. 2015a, *The Astrophysical Journal*, 799, 114,  
 642 doi: [10.1088/0004-637X/799/2/114](https://doi.org/10.1088/0004-637X/799/2/114)
- 643 Hartwig, T., Glover, S. C. O., Klessen, R. S., Latif, M. A.,  
 644 & Volonteri, M. 2015b, *Monthly Notices of the Royal  
 645 Astronomical Society*, 452, 1233,  
 646 doi: [10.1093/mnras/stv1368](https://doi.org/10.1093/mnras/stv1368)
- 647 Johnson, J. L., Khochfar, S., Greif, T. H., & Durier, F.  
 648 2011, *Monthly Notices of the Royal Astronomical Society*,  
 649 410, 919, doi: [10.1111/j.1365-2966.2010.17491.x](https://doi.org/10.1111/j.1365-2966.2010.17491.x)
- 650 Kannan, R., Macciò, A. V., Fontanot, F., et al. 2015,  
 651 *Monthly Notices of the Royal Astronomical Society*, 452,  
 652 4347, doi: [10.1093/mnras/stv1633](https://doi.org/10.1093/mnras/stv1633)
- 653 Kennicutt, R. C. 1998, *Annual Review of Astronomy &  
 654 Astrophysics*, 36, 189,  
 655 doi: [10.1146/annurev.astro.36.1.189](https://doi.org/10.1146/annurev.astro.36.1.189)
- 656 Kennicutt, R. C. J., Calzetti, D., Walter, F., et al. 2007,  
 657 *The Astrophysical Journal*, 671, 333, doi: [10.1086/522300](https://doi.org/10.1086/522300)
- 658 Leroy, A. K., Walter, F., Sandstrom, K., et al. 2013, *The  
 659 Astronomical Journal*, 146, 19,  
 660 doi: [10.1088/0004-6256/146/2/19](https://doi.org/10.1088/0004-6256/146/2/19)
- 661 Planck Collaboration, Ade, P. A. R., Aghanim, N., et al.  
 662 2016, *Astronomy and Astrophysics*, 594, A13,  
 663 doi: [10.1051/0004-6361/201525830](https://doi.org/10.1051/0004-6361/201525830)
- 664 Safranek-Shrader, C., Krumholz, M. R., Kim, C.-G., et al.  
 665 2017, *Monthly Notices of the Royal Astronomical Society*,  
 666 465, 885, doi: [10.1093/mnras/stw2647](https://doi.org/10.1093/mnras/stw2647)
- 667 Schmidt, M. 1959, *The Astrophysical Journal*, 129, 243,  
 668 doi: [10.1086/146614](https://doi.org/10.1086/146614)
- 669 Shang, C., Bryan, G. L., & Haiman, Z. 2010, *Monthly  
 670 Notices of the Royal Astronomical Society*, 402, 1249,  
 671 doi: [10.1111/j.1365-2966.2009.15960.x](https://doi.org/10.1111/j.1365-2966.2009.15960.x)
- 672 Sobolev, V. V. 1957, *Soviet Astronomy*, 1, 678
- 673 Stecher, T. P., & Williams, D. A. 1967, *The Astrophysical  
 674 Journal*, 149, L29, doi: [10.1086/180047](https://doi.org/10.1086/180047)

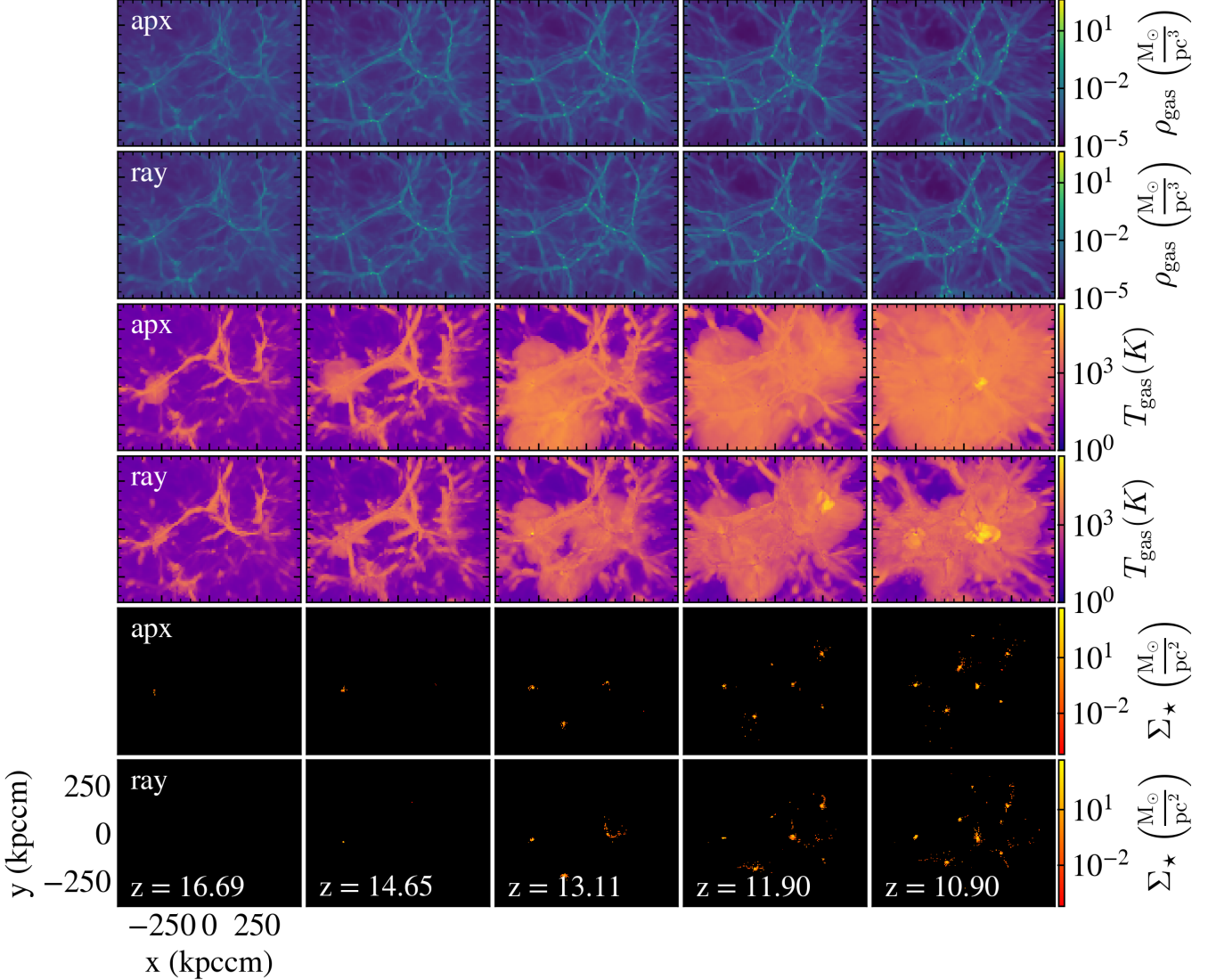


**Figure 9.** The gas surface density, gas temperature, and stellar surface density between the *EarlyRe-apx* and *EarlyRe-ray* simulation.

675 Strawn, C., Roca-Fàbrega, S., Primack, J. R., et al. 2024,  
 676 The Astrophysical Journal, 962, 29,  
 677 doi: [10.3847/1538-4357/ad12cb](https://doi.org/10.3847/1538-4357/ad12cb)

678 Thoul, A. A., & Weinberg, D. H. 1995, The Astrophysical  
 679 Journal, 442, 480, doi: [10.1086/175455](https://doi.org/10.1086/175455)

680 Wise, J. H., & Abel, T. 2011, Monthly Notices of the Royal  
 681 Astronomical Society, 414, 3458,  
 682 doi: [10.1111/j.1365-2966.2011.18646.x](https://doi.org/10.1111/j.1365-2966.2011.18646.x)

683 Wise, J. H., & Cen, R. 2009, The Astrophysical Journal,  
 684 693, 984, doi: [10.1088/0004-637X/693/1/984](https://doi.org/10.1088/0004-637X/693/1/984)

685 Wolcott-Green, J., Haiman, Z., & Bryan, G. L. 2011,  
 686 Monthly Notices of the Royal Astronomical Society, 418,  
 687 838, doi: [10.1111/j.1365-2966.2011.19538.x](https://doi.org/10.1111/j.1365-2966.2011.19538.x)

688 Wong, T., & Blitz, L. 2002, The Astrophysical Journal,  
 689 569, 157, doi: [10.1086/339287](https://doi.org/10.1086/339287)

690 Yoshida, N., Abel, T., Hernquist, L., & Sugiyama, N. 2003,  
 691 The Astrophysical Journal, 592, 645, doi: [10.1086/375810](https://doi.org/10.1086/375810)

692 Yoshida, N., Oh, S. P., Kitayama, T., & Hernquist, L. 2007,  
 693 The Astrophysical Journal, 663, 687, doi: [10.1086/518227](https://doi.org/10.1086/518227)

694 Yoshida, N., Omukai, K., Hernquist, L., & Abel, T. 2006,  
 695 The Astrophysical Journal, 652, 6, doi: [10.1086/507978](https://doi.org/10.1086/507978)

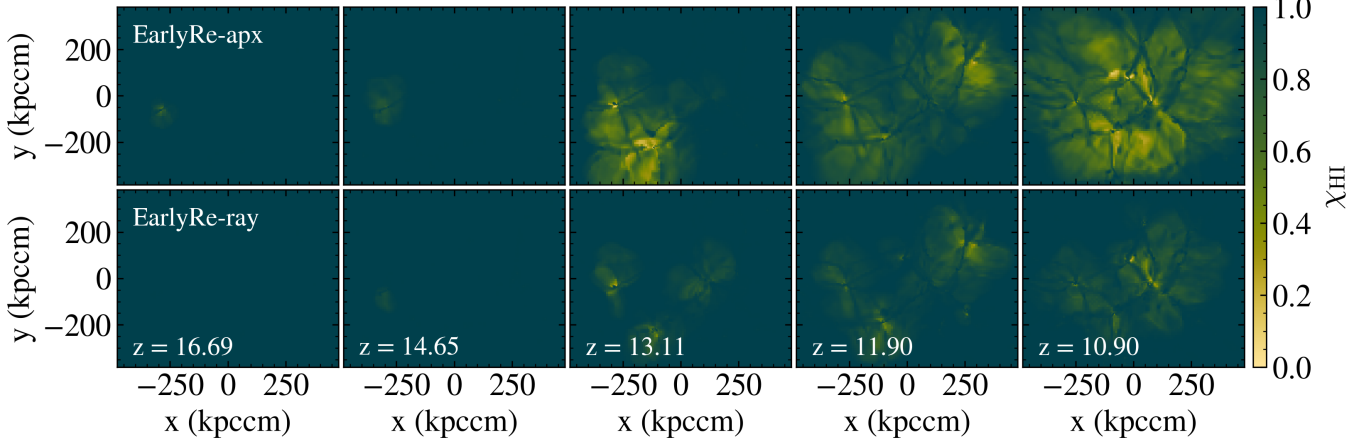


**Figure 10.** The neutral hydrogen fraction in the whole refined region box between the *EarlyRe-ray* and *EarlyRe-apx* simulations.

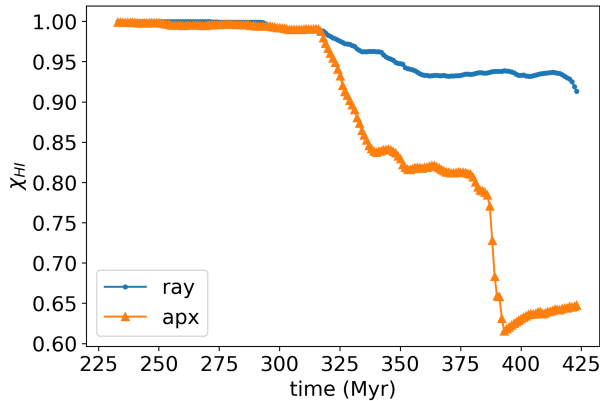


**Figure 11.** The comparison between the volume-weighted average of the neutral hydrogen fraction as a function of time between the *EarlyRe-ray* and the *EarlyRe-apx* simulations.